Journal of Energy Chemistry 26 (2017) 681–687

Contents lists available at ScienceDirect

Journal of Energy Chemistry

journal homepage: www.elsevier.com/locate/jechem

http://www.journals.elsevier.com/journal-of-energy-chemistry/

Morphology and crystal-plane effects of Zr-doped CeO_2 nanocrystals on the epoxidation of styrene with tert-butylhydroperoxide as the oxidant

Jia Ren[a], Xin Liu[a], Ruihua Gao[b,*], Wei-Lin Dai[a,*]

[a] Department of Chemistry & Shanghai Key Laboratory of Molecular Catalysis and Innovative Material, Fudan University, Shanghai 200433, China
[b] State Key Laboratory of Molecular Engineering of Polymers, Department of Macromolecular Science, Fudan University, Shanghai 200433, China

ARTICLE INFO

Article history:
Received 7 November 2016
Revised 26 December 2016
Accepted 22 January 2017
Available online 21 February 2017

Keywords:
Morphology effect
Zr-doped CeO_2
Styrene
Selective oxidation
Oxygen vacancies

ABSTRACT

The morphology effect of Zr-doped CeO_2 was studied in terms of their activities in the selective oxidation of styrene to styrene oxide using tert-butyl hydroperoxide as the oxidant. In the present work, Zr-doped CeO_2 nanorods exhibited the highest catalytic performance (yield of styrene oxide and TOF value) followed by nanoparticles and nanocubes. For the Zr-doped CeO_2 nanorods, the apparent activation energy is 56.3 kJ/mol, which is much lower than the values of catalysts supported on nanoparticles and nanocubes (73.3 and 93.4 kJ/mol). The high resolution transmission electron microscopy results indicated that (1 0 0) and (1 1 0) crystal planes are predominantly exposed for Zr-doped CeO_2 nanorods while (1 0 0) and (1 1 1) for nanocubes, (1 1 1) for nanoparticles. The remarkably increased catalytic activity of the Zr-doped CeO_2 nanorods is mainly attributed to the higher percentage of Ce^{3+} species and more oxygen vacancies, which are associated with their exposed (1 0 0) and (1 1 0) crystal planes. Furthermore, recycling studies proved that the heterogeneous Zr-doped CeO_2 nanorods did not lose its initial high catalytic activity after five successive recycles.

© 2017 Science Press and Dalian Institute of Chemical Physics, Chinese Academy of Sciences. Published by Elsevier B.V. and Science Press. All rights reserved.

1. Introduction

Epoxidation reaction of styrene plays an important role in industrial processes because the products from epoxidation reaction of styrene are versatile intermediates in fine chemicals for the synthesis of perfumes, plasticizers, pharmaceuticals and drugs, etc. [1]. Traditionally, the epoxidation of styrene is carried out by the direct oxidation of alkenes with stoichiometric peracids which produced much waste and byproducts, and even worse, the peracids are corrosive, hazardous to the environment. With growing attention paid to the sustainable development, much more efforts have been made to develop a variety of new processes of styrene epoxidation using H_2O_2, urea-H_2O_2 or TBHP as oxidants with the catalysts such as TS-1 [8], Ti-SiO_2 [9], Ti-HMS [10], as well as γ-Al_2O_3 [11]. Meanwhile, the separable solid catalysts, such as Mo [2], Fe [3], Mn [4], Co [5], Cu [6] and Ni [7] based catalysts, were proven to be efficient in the epoxidation of styrene. However, the catalysts mentioned above exhibited comparatively unsatisfied epoxide selectivity or low activity [8–11].

As a well-known functional rare earth material, ceria has been widely applied in the fields of industrial heterogeneous catalysts, such as automotive three-way exhaust (TWCs) [12], water-gas-shift (WGS) reactions [13], solid oxide fuel cells anodes (SOFCs) [14]. In order to promote the physical and chemical properties of CeO_2, incorporation of cheaper transition metals such as Mn, Fe, Co, Ni, and Zr by doping approach is a suitable option because of the low cost and strong stability of transition metals against poisoning. For example, recently, Chen et al. [15] reported the shape effect of $Ce_{1-x}Zr_xO_2$ nanorods in terms of redox features and catalytic activity in CO oxidation. Besides, other groups reported that CeO_2–CuO nanomaterials showed high catalytic activity when compared with pure CeO_2 [16]. The insertion of Zr into ceria lattice leads to structural distortions of the cubic fluorite lattice compared with pure CeO_2, ultimately resulting in the enhancement of mobility of lattice oxygen and the density of oxygen vacancies. CeO_2 in a cubic fluorite structure possesses three low-index planes: (1 1 0), (1 1 1) and (1 0 0); the (1 1 1) plane is the most stable, followed by (1 1 0) and (1 0 0) facets [17–19]. As we know, ceria catalysts with different morphologies were established to possess different crystal planes and surface properties [20], which can influence the interaction between ceria surface and the adsorbed reactants. For instance, Zhou et al. found that CeO_2 nanorods showed better

* Corresponding authors.
E-mail addresses: ruihuagao@fudan.edu.cn (R. Gao), wldai@fudan.edu.cn (W.-L. Dai).

http://dx.doi.org/10.1016/j.jechem.2017.01.007
2095-4956/© 2017 Science Press and Dalian Institute of Chemical Physics, Chinese Academy of Sciences. Published by Elsevier B.V. and Science Press. All rights reserved.

catalytic performance in CO oxidation than irregular nanoparticles because of the exposed reactive crystal planes [17]. Moraes et al. reported the effects of ceria morphology on catalytic performance of Ni/CeO_2 for the low temperature steam reforming of ethanol and found that Ni supported on ceria nanocubes had the best performance [21]. Fan et al. found that spindle-like CeO_2 showed a higher catalytic activity on CO conversion [22]. So far, the morphology dependence on Zr-doped CeO_2 nanomaterials for the epoxidation reaction of styrene has been rarely reported yet.

In our previous work, the CeO_2 nanorods with various Zr dopant concentrations catalysts are prepared and investigated in terms of their catalytic activities in catalyzing styrene oxidation [23]. In the present work, Zr-doped CeO_2 catalysts of different morphologies are further investigated in terms of their activities in catalyzing the styrene oxidation reaction. The structure of the Zr-doped CeO_2 is studied using various techniques including Brunauer–Emmett–Teller (BET) method, X-ray diffraction (XRD), transmission electron microscopy (TEM), high-resolution transmission electronmicroscopy (HRTEM), Raman spectroscopy, and X-ray photoelectron spectroscopy (XPS) in order to investigate the relationship between the morphology and the catalytic activity. It is found that the morphology has a great influence on the exposed crystal planes, oxygen vacancy concentrations and the content of Ce^{3+} ions, which contribute to the variation of the catalytic activity in styrene oxidation reaction.

2. Experimental

2.1. Catalyst preparation

All the materials were purchased from Sinopharm Chemical Reagent Co., Ltd. China. All chemicals were used without further purification. Deionized water was used throughout the experiments.

Zr-doped CeO_2 nanorods, Zr-doped CeO_2 nanocubes, and Zr-doped CeO_2 nanoparticles were prepared by a hydrothermal method varying the amount of reactant and hydrothermal temperature. The theoretical molar ratios of Zr/(Zr+Ce) over the Zr-doped CeO_2 were all about 10%. Typically, 4.5 mmol of $Ce(NO_3)_3{\bullet}6H_2O$, 0.5 mmol of $Zr(NO_3)_4{\bullet}5H_2O$, and an appropriate amount of NaOH (19.2 g for nanorods and nanocubes, 0.32 g for nanoparticles) were dissolved into 40 mL of distilled water, respectively. Then, the solution was mixed together and kept stirring for 30 min. The mixture was then transferred to a stainless steel reaction tank with polytetrafluoroethylene (PTFE) lining (100 mL) and maintained at an appropriate temperature (373 K for nanorods, 453 K for nanocubes and nanoparticles) for 24 h. After centrifugation and washing with water and ethanol, the precipitate was dried at 353 K overnight, and finally calcined at 673 K for 5 h in air with the ramping rate of 2 °C/min. The as-prepared Zr-doped CeO_2 nanorods, Zr-doped CeO_2 nanoparticles and Zr-doped CeO_2 nanocubes were respectively denoted as Zr-doped CeO_2 NR, Zr-doped CeO_2 NP and Zr-doped CeO_2 NC.

2.2. Characterizations

XRD patterns were obtained on a Bruker D8 advance spectrometer with Cu *Kα* radiation ($\lambda = 0.154$ nm), operated at 40 mA and 40 kV, respectively. The lattice parameter *a* value was calculated using the Scherrer equation. TEM images were performed on a JOEL JEM 2010 transmission electron microscope. The samples were supported on carbon-coated copper grids for the experiment. XPS was performed using a RBD 147 upgraded Perkin Elmer PHI 5000C ESCA system equipped with a dual X-ray source, of which the Mg *Kα* (1253.6 eV) anode and a hemispherical energy analyzer was used. The background pressure during data acquisition was maintained at $<10^{-6}$ Pa. Measurements were performed at a pass energy of 93.90 eV. All binding energies were calibrated using contaminant carbon (C $1s = 284.6$ eV). The actual composition of the catalysts was determined by Optima 8000 ICP-OES Spectrometer. The laser Raman experiments were obtained using a Jobin Yvon Dilor Labram I Raman spectrometer equipped with a charge coupled device detector, holographic notch filter, and the He-Ne laser radiating at 632.8 nm. Specific surface areas of the catalysts were measured by nitrogen adsorption-desorption at 77 K (Micromeritics Tristar ASAP 3000) employing the BET method. The sample was pre-treated at 523 K in vacuum for 3 h before test to degas the adsorbed moisture.

2.3. Activity test

The epoxidation of styrene was carried out at reflux oil bath temperature of 353 K in a closed 25 mL regular glass reactor with magnetically stirred (400 r/min) using 70 wt% aqueous *t*-butyl hydroperoxide (TBHP) as the oxidant and acetonitrile as solvent. First, 0.05 g of the catalyst, 8.7 mmol of 70 wt% aqueous TBHP and 10 mL of acetonitrile were introduced into the regular glass reactor at 353 K with magnetic stirring. Then, 4.35 mmol of styrene was added into the above mixture to start the reaction and the mixture was maintained for a period of time. Gas chromatography (GC) was used to carry out the quantitative analysis of the reaction products, and GC-mass spectroscopy (GC-MS) was applied to determine different products in the reaction mixture.

Substrate conversion = moles of substrate converted/moles of substrate used;

Product selectivity = moles of product formed/moles of substrate converted;

The stability was tested as follows: the catalyst was separated by centrifuge, washed by water and ethanol for several times, and dried under 353 K for 12 h.

3. Results and discussion

3.1. Characterization of the as-prepared material

The morphology of the synthesized Zr-doped CeO_2 nanoparticles, Zr-doped CeO_2 nanorods, and Zr-doped CeO_2 nanocubes are investigated by TEM and HRTEM as shown in Fig 1. As presented in Fig 1(a), Zr-doped CeO_2 nanoparticles are uniformly distributed and established to be around 10 nm in diameter. Fig 1(b) depicts a high revolution TEM image of Zr-doped CeO_2 nanoparticles with a fast Fourier transform analysis (inset). According to the HRTEM image, the dominating (1 1 1) planes are observed with an interplanar spacing of 0.32 nm, being accorded well with the previous report [24]. For the Zr-doped CeO_2 nanorods, the measured size is approximate with 30–80 nm in length and 10 ± 1 nm in diameter as shown in Fig 1(c). Meanwhile, (1 0 0) and (1 1 0) crystal planes are predominantly exposed with an interplanar spacing of 0.26 and 0.19 nm according to its HRTEM image. For the Zr-doped CeO_2 nanocubes exhibited in Fig. 1(e) and (f), the diameter distribution is about 60–80 nm. At the same time, a small number of (1 0 0) planes and the dominating (1 1 1) planes are observed with an interplanar spacing of 0.27 and 0.32 nm. Some light points on the ceria are observed from the HRTEM image in Fig. 1(b), (d), (f), revealing the existence of the surface defects. Theoretical studies have shown that (1 1 1) is the least active surface followed by (1 0 0) and (1 1 0), in which the energy needed to produce oxygen vacancy is inverse proportional to the order of the reactivity of crystal planes [25–27]. Thus, according to the exposed crystal planes of Zr-doped CeO_2 of different morphologies observed in HRTEM image, the Zr-doped CeO_2 nanorods exhibited the highest concentration of surface oxygen vacancies, followed by Zr-doped

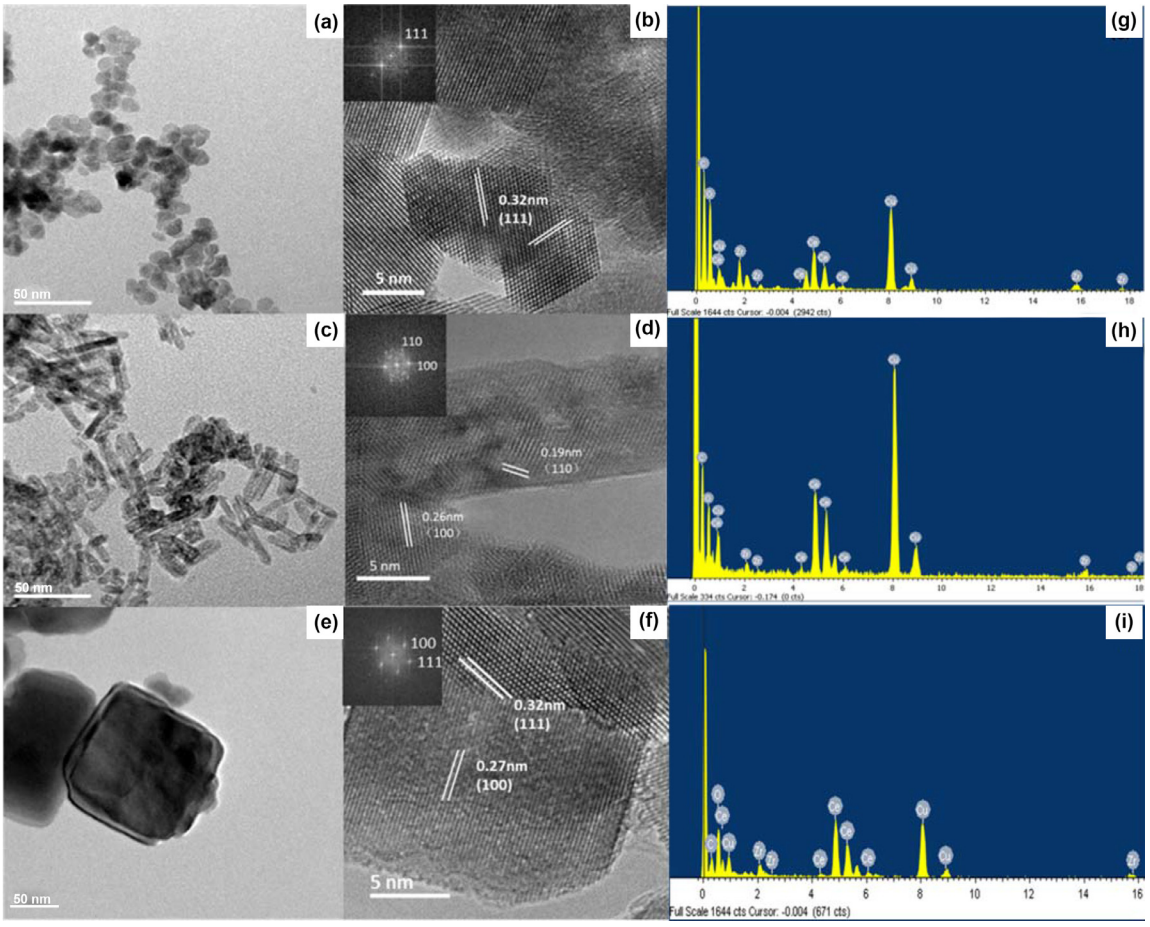

Fig. 1. TEM images of Zr-doped CeO_2 (a) nanoparticles, (c) nanorods, and (e) nanocubes. HRTEM image of Zr-doped CeO_2 (b) nanoparticles, (d) nanorods, and (f) nanocubes. EDS patterns of Zr-doped CeO_2 (g) nanoparticles, (h) nanorods, and (i) nanocubes.

CeO_2 nanocubes and nanoparticles. The EDS spectra in Fig. 1(g), (h), (i) confirm the presence of elements Ce, Zr and O (the Cu element is from the substrates), which indicated the homogeneity of the obtained catalysts.

The crystal structures of the as-synthesized Zr-doped CeO_2 nanorods, Zr-doped CeO_2 nanoparticles, and Zr-doped CeO_2 nanocubes are investigated by XRD techniques and shown in Fig. 2. The diffraction peaks at 28.5°, 33.0°, 47.5°, 56.3° and 59.1° assigned to the (1 1 1), (2 0 0), (2 2 0), (3 1 1) and (2 2 2) planes are indexed to the cubic fluorite structure of CeO_2 crystals (JCPDS no. 34-0394). The peaks indexed to zirconium oxide are not detected in all the samples, indicating that Zr was successfully incorporated into the ceria lattice structure. As shown in Fig. 2, the nanocubes exhibit the sharpest peaks with the highest intensity, indicating their well-developed crystallinity and large grain size, in agreement with the TEM results. Besides that, the calculated lattice parameter values for pure CeO_2 [23], Zr-doped CeO_2 nanorods, Zr-doped CeO_2 nanoparticles, Zr-doped CeO_2 nanocubes are 5.448 Å, 5.395 Å, 5.394 Å, and 5.391 Å, respectively. We can see that the lattice parameter (a) of Zr-doped CeO_2 of different morphologies decreased compared to pure CeO_2, and this decrease is mainly due to the replacement of Ce^{4+} (0.97 Å) by slightly smaller radius of Zr^{4+} (0.84 Å). These XRD results further confirm the incorporation of Zr into the ceria lattice to form fluorite-like solid solutions.

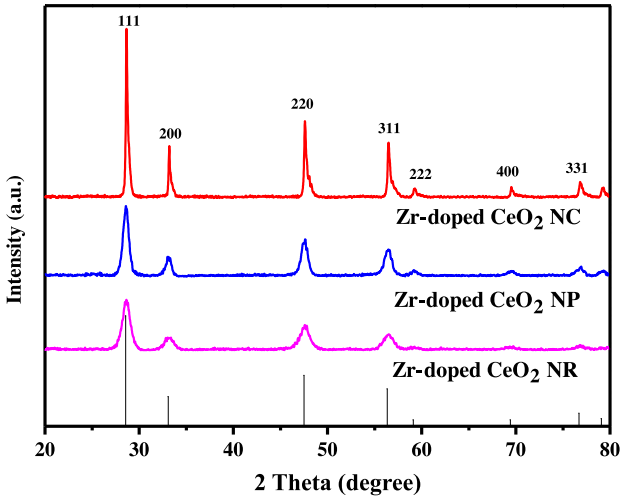

Fig. 2. XRD patterns of as-prepared Zr-doped CeO_2 of different morphologies.

Raman spectroscopy is considered to be a very efficient and non-destructive technique for characterizations of oxygen vacancies. The Raman spectra of Zr-doped CeO_2 of different morphologies are compared in Fig. 3(a). A strong Raman shift at ~460 nm and a relatively weak shift at ~600 nm can be detected. The shift at ~460 nm is assigned to distinct F_{2g} symmetry mode of the CeO_2 phase [27,28]. Besides the band at 460 cm^{-1}, the band at 600 cm^{-1} is assigned to the non-degenerate longitudinal optical (LO) mode [29], which is related to the oxygen vacancies caused by the Ce^{3+} ion in the lattice and the small size effects [30]. According to the previous work, small cerium ions show Ce^{3+} tervalence, and in order to maintain the particles in an electrically neutral state, the lattice oxygen would escape from the structure and finally result in the formation of intrinsic oxygen vacancies, which are very

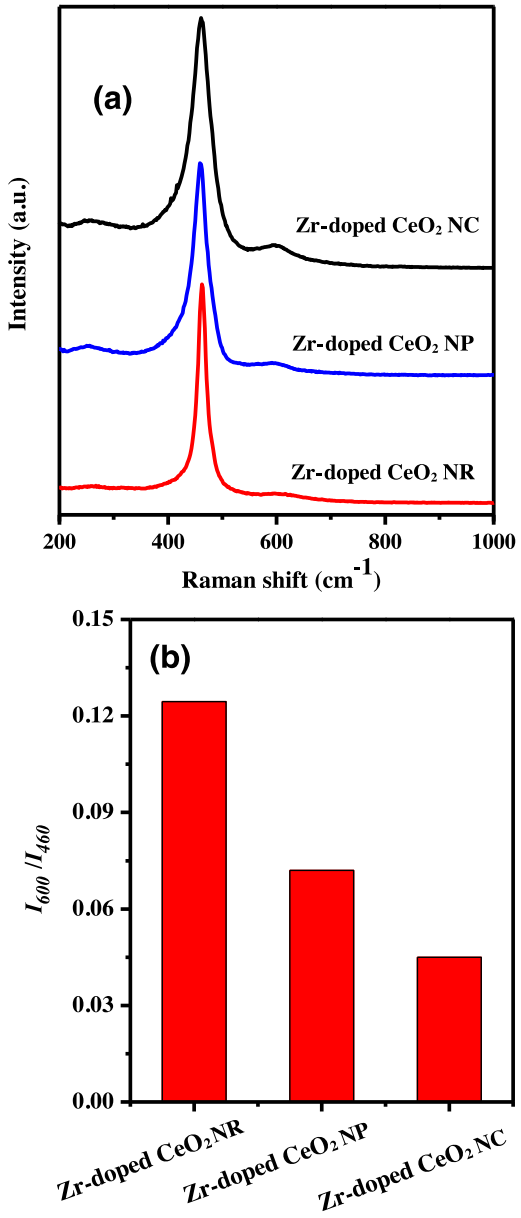

Fig. 3. (a) Raman spectra of Zr-doped CeO_2 of different morphologies, (b) the corresponding peak intensity ratio of I_{600}/I_{460}.

important for the excitation of the oxygen in substrates in the catalytic reactions. Importantly, the I_{600}/I_{460} values (Fig. 3b), which indicate the defect concentration, such as concentration of oxygen vacancies, reveal a difference among Zr-doped CeO_2 of different morphologies. The I_{600}/I_{460} value of Zr-doped CeO_2 nanorods calculated by the Raman spectra established to be the highest, and Zr-doped CeO_2 nanoparticles and nanocubes followed in sequence, which indicated that the concentration of oxygen vacancies of Zr-doped CeO_2 nanorods reached the highest if compared to nanoparticles and nanocubes.

The Ce 3*d* and O 1*s* XPS spectra of the Zr-doped CeO_2 nanorods, Zr-doped CeO_2 nanoparticles, and Zr-doped CeO_2 nanocubes are shown in Fig. 4, and the relative element content of Zr-doped CeO_2 determined are shown on Table 1. The Ce 3*d* spectra in Fig. 4(a) have been fitted into eight peaks: ν (~881.4 eV), ν' (~884.7 eV), ν'' (~888.1 eV), ν''' (~897.3 eV), μ (~900.0 eV), μ′ (~902.8 eV), μ″ (~906.6 eV) and μ‴ (~915.7 eV). The four μ bands represent the Ce $3d^{3/2}$, and the other four ν bands represent the Ce $3d^{5/2}$ [31]. The $3d^{10}4f^0$ state of Ce^{4+} species are labeled as μ, μ″, μ‴, ν, ν'', and ν''', whereas the $3d^{10}4f^1$ state of Ce^{3+} are labeled as μ′ and ν' [32]. From Fig 4(a), it is obvious that the Ce^{+4} oxidation state is the main chemical valence of cerium on the surface, co-existing a small amount of Ce^{+3} oxidation state which was introduced by the spontaneous transformation of Ce^{4+} (0.97 Å) to the larger Ce^{3+} (1.10 Å) [33]. Oxygen vacancies can be produced by the transformation between Ce^{3+} and Ce^{4+} as below,

$$4Ce^{4+}+O^{2-} \rightarrow 4Ce^{4+}+2e^-/\square+0.5O_2 \rightarrow 2Ce^{4+}+2Ce^{3+} +\square+0.5O_2$$

(□ represents an empty position)

The percentages of Ce^{3+} to the total Ce are 19.5%, 16.4% and 8.5% for the catalysts of Zr-doped CeO_2 nanorods, nanoparticles and nanocubes, respectively. The higher the Ce^{3+} concentration of the total Ce that exists, the more oxygen vacancies that form. Therefore, the concentration of the oxygen vacancies of Zr-doped CeO_2 nanorods reaches the maximum value.

The O 1*s* bands of Zr-doped CeO_2 of different morphologies are shown in Fig. 4(b). The sub-bands at lower binding energy (~528.5 eV) corresponded to the lattice oxygen (O_L); (~530.7 eV) corresponded to the weakly bonded oxygen species and/or chemisorbed oxygen (O_C); the highest binding energy (~532.6 eV) corresponded to the surface absorbed oxygen (O_S), such as O_2^{2-}, or O^- belonging to defect oxide or

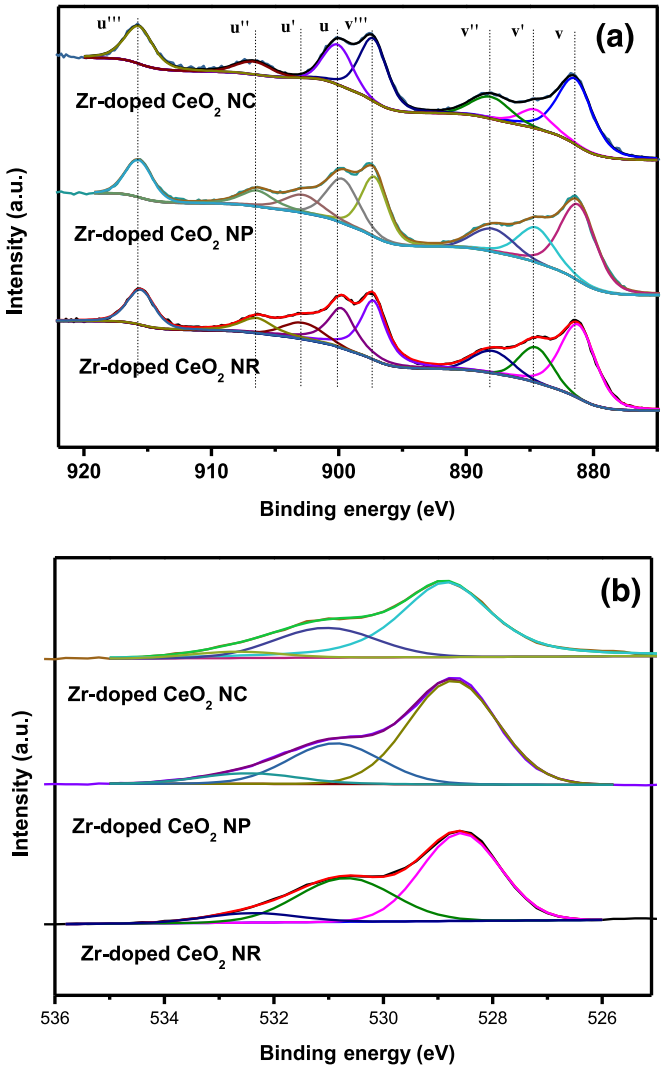

Fig. 4. (a) Ce 3*d* and (b) O 1*s* XPS spectra of Zr-doped CeO_2 of different morphologies.

Table 1. The surface area and atomic ratios of the different catalysts.

Catalyst	$Ce^{3+}/(Ce^{4+}+Ce^{3+})$[a]	Zr/(Zr+Ce)[a]	Zr/(Zr+Ce)[b]	S_{BET} (m^2/g)	O_α/O_T	Crystal planes
Zr-doped CeO_2 NR	19.1%	11.8%	8.9%	103.9	42.3%	(110), (100)
Zr-doped CeO_2 NP	16.4%	13.8%	8.4%	117.5	34.4%	(111)
Zr-doped CeO_2 NC	8.5%	25.8%	8.7%	6.5	29.6%	(100), (111)

[a] Determined by XPS,
[b] Determined by ICP

hydroxyl-like group [34,35]. As shown in Table 1, the ratio of O_α to O_T ($O_T=O_L+O_C+O_S$, $O_\alpha=O_C+O_S$) for all samples was calculated. It is obvious that the morphology of Zr-doped CeO_2 can effectively influence the active oxygen sites (O_α) on the surface. The ratio of the active oxygen sites on the surface are 42.3%, 34.4%, and 29.6% for nanorods, nanoparticles and nanocubes, respectively. At the same time, it is obvious that the concentration of lattice oxygen (O_L) is diverse among the different morphologies (nanorods: 57.7%; nanoparticles: 65.6%; nanocubes: 70.4%) and the consummation of lattice oxygen indicates the formation of oxygen vacancies which are very important in the catalytic reactions.

3.2. Catalytic oxidation of styrene

3.2.1. Catalytic activity of the Zr-doped CeO_2 of different morphologies

The morphology effect of the catalytic activity of Zr-doped CeO_2 was firstly evaluated in the oxidation of styrene to styrene oxide using 70% TBHP as the oxidant and acetonitrile as the solvent. The catalytic activities of Zr-doped CeO_2 of different morphologies are summarized in Table 2. The styrene conversion is 5.4% when the reaction is carried out without any catalysts, according to the auto-oxidation of the styrene by THBP. Also, pure CeO_2 or ZrO_2 shows a low styrene conversion about 32%. Among the Zr-doped CeO_2 of different morphologies, the Zr-doped CeO_2 nanorods exhibit the highest activity with 78.1% styrene conversion and 79.3% selectivity for styrene oxide with the highest TOF (7.656 h^{-1}) as well, followed by nanoparticles and nanocubes as shown in Table S1. This finding can be ascribed to the crystal plane effect, the higher percentage of Ce^{3+} species and the oxygen vacancies concentration which were supported by the above analysis results. The main exposed crystal planes of Zr-doped CeO_2 nanorods is (1 1 0) while more stable crystal planes (1 1 1) is dominated for Zr-doped CeO_2 nanoparticles. From the previous research, the stability order of the three different crystal planes is established to be (1 1 1)>(1 0 0)>(1 1 0) [36], and the more unstable the crystal plane is, the more oxygen vacancies it can produce [37]. Oxygen vacancies, which play a key role in the catalytic reactions, could activate the oxygen species in the reaction system to accelerate the catalytic process. At the same time, besides oxygen vacancies, the coordination ability of Ce-cation can influence the catalytic performance of Ce-based catalysts and it is established that Ce-cation on the (1 1 0) crystal planes has a better ability of coordination [38]. Thus, for the Zr-doped CeO_2 of different morphologies, the concentration of oxygen vacancies and the percentages of Ce^{3+} to the total Ce species are the highest for nanorods, which is consistent with the reaction activity order. The catalytic activity of Zr-doped CeO_2 nanocubes is lower than that of nanoparticles, while the dominated exposed crystal plane of nanocubes is (1 0 0) which is the more activated. This activity difference may be due to the fact that the size of nanocubes is too big and the surface area is too small, leading to the lower absolute concentration of oxygen vacancies and less activated sites on the nanocubes catalyst.

Table 2. Catalytic performance of styrene epoxidation over different catalysts[a].

Catalysts	Styrene conversion (%)	Selectivity of styrene oxide (%)	Yield (%)
Zr-doped CeO_2 NR	78.1	79.3	61.9
Zr-doped CeO_2 NP	69.5	81.1	56.3
Zr-doped CeO_2 NC	44.6	88.5	39.5
ZrO_2	32.7	82.6	27.0
CeO_2	32.2	83.1	26.8
ZrO_2+CeO_2[b]	32.2	82.2	26.5
Zr-doped CeO_2[c]	55.5	80.3	44.6
Blank[d]	5.4	81.0	4.4

[a] Reaction conditions: 50 mg catalyst, 4.35 mmol styrene, 8.7 mmol TBHP (70% aqueous solution), solvent (CH_3CN) = 5 mL, reaction temperature 80 °C, reaction time 12 h.
[b] The ZrO_2+CeO_2 (mol ratio of Ce/Zr = 9) was fabricated by a physical mixing method.
[c] The Zr-doped CeO_2 was prepared by traditional precipitate process, with no specific morphology.
[d] Without catalyst.

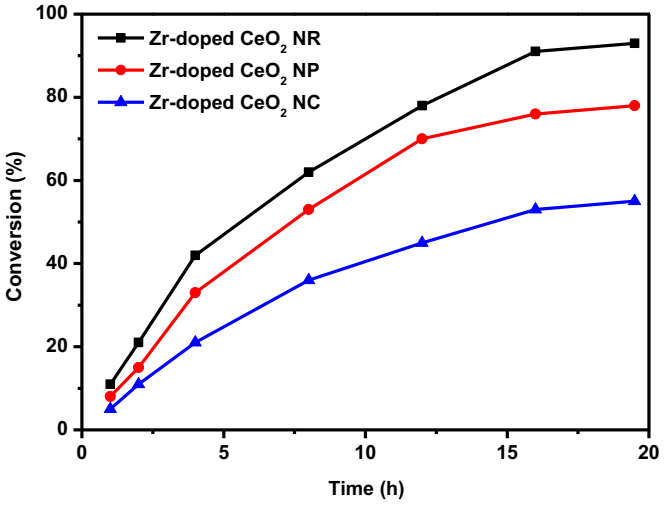

Fig. 5. Time-dependence evolution of styrene conversion for Zr-doped CeO_2 of different morphologies.
[a]Reaction conditions: 50 mg catalyst, 4.35 mmol styrene, 8.7 mmol TBHP (70% aqueous solution), solvent (CH_3CN) = 5 mL, reaction temperature 80 °C.

The effect of reaction time on the conversion of styrene for Zr-doped CeO_2 of different morphologies is also described in Fig. 5. For nanorods, the conversion of styrene is 21.0% in the first 2 h and then increased to 78.1% with the reaction time prolonging to 12 h, while the nanoparticles and nanocubes show the similar trend during the reaction time.

Fig. 6 shows the Arrhenius plots based on the reaction rate data between 50 °C and 80 °C. The apparent activation energy is determined from these plots based on Eq. (1) and given in Table 3.

$$K = A\exp(-E_a/RT) \quad (1)$$

Table 3. Apparent activation energy comparison of the Zr-doped CeO_2 of different morphologies.

Catalysts	E_a (kJ/mol)
Zr-doped CeO_2 NC	93.4
Zr-doped CeO_2 NP	73.3
Zr-doped CeO_2 NR	56.3

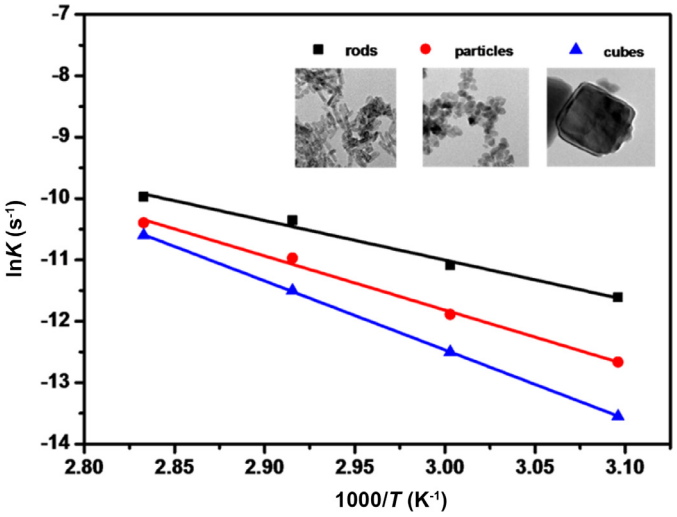

Fig. 6. Apparent activation energy comparison of the Zr-doped CeO_2 of different morphologies.

where A is the pre-exponential factor, E_a is the apparent activation energy (kJ/mol), R is the gas constant (8.3145 J/mol/K) and T is the temperature (K).

For the Zr-doped CeO_2 nanorods, the apparent activation energy is 56.3 kJ/mol, which is much lower than the values of nanoparticles and nanocubes (73.3 and 93.4 kJ/mol). Therefore, the catalytic activity of Zr-doped CeO_2 nanorods was higher than that of nanoparticles and nanocubes catalysts.

On the basis of the earlier reports [[39],42] and our experiment results, the possible catalytic mechanism of the Zr-doped CeO_2 of different morphologies is proposed. In brief, the Ce^{3+} ions coupled with the large sized oxygen vacancy clusters are surface active sites, promoting the adsorption of styrene on the surface of catalysts. The styrene is first absorbed on the surface of Zr-doped CeO_2 nanomaterials through the π-electron interactions. Then the oxygen vacancies activate THBP in the reaction system to activated oxygen species which can react with the styrene absorbed to produce styrene oxide and leave oxygen vacancies. The oxygen vacancies are then replenished by the TBHP, thus completing the reaction cycle. Obviously, among the different morphologies, the nanorods with the highest ratio of $Ce^{3+}/(Ce^{3+}+Ce^{4+})$ show the best catalytic performance due to the highest concentration of Ce^{3+} and oxygen vacancies.

3.2.2. Catalyst reusability

The practical reusability of the Zr-doped CeO_2 nanorods in the epoxidation of styrene was tested to evaluate the stability of the catalyst on behalf of Zr-doped CeO_2 of different morphologies. The recycling test was performed for continuous five reaction cycles under the identical reaction as mentioned above. From Fig. 7(a), the Zr-doped CeO_2 nanorods catalyst showed good stability for the epoxidation reaction in successive five runs. The stability was further confirmed by XRD patterns (Fig. 7b) of the Zr-doped CeO_2 nanorods before and after five reaction recycles.

4. Conclusions

In summary, the Zr-doped CeO_2 of different morphologies, including nanorods, nanoparticles and nanocubes, were synthesized via a facile simple hydrothermal method. According to a series of characterization analysis, the Zr-doped CeO_2 of different morphologies possessed different surface structures, which dramatically influence the catalytic performance in the epoxidation of styrene. A correlation between different crystal morphology of Zr-doped CeO_2 on the structure and catalytic performance was established. The Zr-doped CeO_2 nanorods were found to possess the best catalytic performance for the selective oxidation of styrene to styrene oxide, followed by nanoparticles and nanocubes. On the Zr-doped CeO_2 nanorods, the apparent activation energy is 56.3 kJ/mol, which is much lower than the values of nanoparticles and nanocubes (73.3 and 93.4 kJ/mol). The HRTEM results indicated that (1 0 0) and (1 1 0) crystal planes are predominantly exposed for Zr-doped CeO_2 nanorods. The results indicated that the large sized oxygen vacancy clusters on (1 1 1) plane, and high percentage of Ce^{3+} associated with them can efficiently improve the catalytic efficiency of styrene epoxidation. This work suggests that the catalyst could be designed to be a suitable morphology to predominately expose active planes to improve the catalytic performance. At the same time, the hydrothermal synthesis method is of easy control and environmental, which is helpful for its further industrial applications.

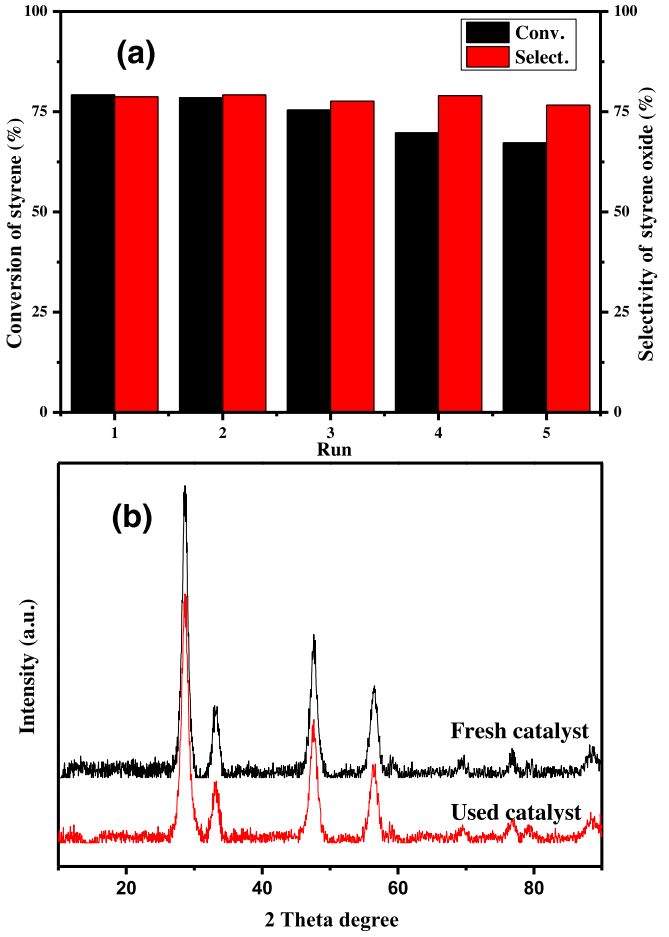

Fig. 7. (a) Recyclability test of Zr-doped CeO_2 nanorods for epoxidation of styrene, (b) XRD patterns of Zr-doped CeO_2 nanorods before and after used and TEM image of nanorods after used.
[a]Reaction conditions: 50 mg catalyst, 4.35 mmol styrene, 8.7 mmol TBHP (70% aqueous solution), solvent (CH_3CN) = 5 mL, reaction temperature 80 °C, reaction time 12 h.

Acknowledgments

We thank the financial support from NNSFC (Project 21373054, 21303023, 21173052), and the Natural Science Foundation of Shanghai Science and Technology Committee (08DZ2270500).

Supplementary materials

Supplementary material associated with this article can be found, in the online version, at doi:10.1016/j.jechem.2017.01.007.

References

[1] J. Sebastian, K.M. Jinka, R.V. Jasra, J. Catal. 244 (2006) 208–218.
[2] B. Wang, J. Zhang, X. Zou, H.G. Dong, P.J. Yao, Chem. Eng. J. 260 (2015) 172–177.
[3] Y. Wang, Q.H. Zhang, T. Shishido, K. Takehira, J. Catal. 209 (2002) 186–196.
[4] Q.H. Zhang, Y. Wang, S. Itsuki, T. Shishido, K. Takehira, J. Mol. Catal. A: Chem. 188 (2002) 189–200.
[5] M. Rocha, S.L.H. Rebelo, C. Freire, Appl. Catal. A: Gen. 460 (2013) 116–123.
[6] B. Li, X. Jin, Y. Zhu, L. Chen, Z. Zhang, X. Wang, Inorg. Chim. Acta 419 (2014) 66–72.
[7] M. Nandi, P. Roy, H. Uyama, A. Bhaumik, Dalton Trans 40 (2011) 12510–12518.
[8] S.C. Laha, R. Kumar, J. Catal. 204 (2001) 64–70.
[9] Q. Yang, S. Wang, J. Lu, G. Xiong, Z. Feng, Q. Xin, C. Li, Appl. Catal. A: Gen. 194–195 (2000) 507–514.
[10] J.S. Sotelo, R. Van Grieken, C. Martos, Chem. Commun (1999) 549–550.
[11] V.R. Choudhary, N.S. Patil, S.K. Bhargava, Catal. Lett. 89 (2003) 55–62.
[12] J. Kaspar, P. Fornasiero, M. Graziani, Catal. Today 50 (1999) 285–298.
[13] Q. Fu, H. Saltsburg, M. Flytzani-Stephanopoulos, Science 301 (2003) 935–938.
[14] C.W. Sun, Z. Xie, C.R. Xia, H. Li, L.Q. Chen, Electrochem. Commun. 8 (2006) 833–838.
[15] A. Chen, Y. Zhou, N. Ta, Y. Li, W. Shen, Catal. Sci. Technol. 5 (2015) 4184–4192.
[16] G. Chen, Q. Xu, Y. Yang, C. Li, T. Huang, G. Sun, S. Zhang, D. Ma, X. Li, ACS Appl. Mater. Interfaces 7 (2015) 23538–23544.
[17] Y. Zhou, S. Wang, M. Xiao, D. Han, Y. Lu, Y. Meng, RSC Adv. 2 (2012) 6831–6837.
[18] L. Liu, Y. Cao, W. Sun, Z. Yao, B. Liu, F. Gao, L. Dong, Catal. Today 175 (2011) 48–54.
[19] C. Binet, M. Daturi, J.C. Lavalley, Catal. Today 50 (1999) 207–225.
[20] N.V. Skorodumova, M. Baudin, K. Hermansson, Phys. Rev. B: Condens. Matter Mater. Phys. 69 (2004) 375–401.
[21] T.S. Moraes, R.C.R. Neto, M.C. Ribeiro, Top Catal. 58 (2015) 281–294.
[22] T. Fan, L.X. Zhang, H.F. Jiu, Y.X. Sun, G.D. Liu, Y.Y. Sun, Q.L. Su, Micro & Nano. Lett. 5 (2010) 230–233.
[23] X. Liu, J. Ding, X. Lin, R.H. Gao, Z.H. Li, W.L. Dai, Appl. Catal. A: Gen. 503 (2015) 117–123.
[24] S.P. Wang, L.F. Zhao, W. Wang, Y. Zhao, G. Zhang, X. Ma, J. Gong, Nanoscale 5 (2013) 5582–5589.
[25] T.X.T. Sayle, S.C. Parker, C.R.A. Catlow, Surf. Sci. 316 (1994) 329–336.
[26] B.C. Zhang, X.L. Tang, Y. Li, W. Cai, Y. Xu, W. Shen, Catal. Commun 7 (2006) 367–372.
[27] S. Thi, X.T. Parker, S.C. Sayle, Phys. Chem. Chem. Phys 7 (2005) 2936–2941.
[28] J.R. McBride, K.C. Hass, B.D. Poindexter, W.H. Weber, J. Appl. Phys. 76 (1994) 2435–2441.
[29] X.M. Lin, L.P. Li, G.S. Li, W.H. Su, Mater. Chem. Phys. 69 (2001) 236–240.
[30] Y. Goto, K. Takahashi, T. Omata, T. Otsuka-Yao-Matsuo, J. Phys.: Conf. Ser. 165 (2009) 1–4.
[31] P. Burroughs, A. Hamnett, A.F. Orchard, G. Thornton, J. Chem. Soc., Dalton Trans 17 (1976) 1686–1698.
[32] B.M. Reddy, A. Khan, Y. Yamada, T. Kobayashi, S. Loridant, J.C. Volta, Langmuir 19 (2003) 3025–3030.
[33] W. Cai, Q. Zhong, W. Zhao, Y. Bu, Appl. Catal. B: Environ 158–159 (2014) 258–268.
[34] J. Yu, Z. Si, L. Chen, X. Wu, D. Weng, Appl. Catal. B: Environ. 163 (2015) 223–232.
[35] Y. Wang, F. Wang, Y. Chen, D. Zhang, B. Li, S. Kang, X. Li, L. Cui, Appl. Catal. B: Environ. 147 (2014) 602–609.
[36] Z.L. Wang, X.D. Feng, J. Phys. Chem. B107 (2003) 13563−13566.
[37] G. Vicario, G Balducci, S. Fabris, S. de Gironcoli, S. Baroni, J. Phys. Chem. B 110 (2006) 19380–19385.
[38] Z.L. Wu, M.J. Li, D. Mullins, S.H. Overbury, ACS Catal 2 (2012) 2224–2234.
[39] X.W. Liu, K.B. Zhou, L. Wang, B.Y. Wang, Y.D. Li, J. Am. Chem. Soc. 131 (2009) 3140–3141.